

QUANTUM DOT INFRARED DETECTORS AND SOURCES

P. BHATTACHARYA and A. D. STIFF-ROBERTS

*Solid State Electronics Laboratory,
Department of Electrical Engineering and Computer Science,
University of Michigan, Ann Arbor, MI 48109-2122, USA*

SANJAY KRISHNA

*Center for High Technology Materials,
Department of Electrical Engineering and Computer Engineering,
University of New Mexico, Albuquerque, NM 87106, USA*

S. KENNERLY

*Sensors and Electron Devices Directorate,
US Army Research Laboratory,
Adelphi, Maryland 20783, USA*

InAs/GaAs quantum dot devices have the potential to be the leading technology for infrared detection and emission, which are necessary for many military and domestic applications. Quantum dot infrared photodetectors yield higher operating temperatures, lower dark currents, and more wavelength tunability. They also permit the detection of normal-incidence light. Quantum dot infrared sources are also expected to yield higher operating temperatures, in addition to lower threshold currents and higher modulation bandwidths. After a brief review of the history of infrared detection and emission, the optical and electrical characteristics of self-organized In(Ga)As/GaAs quantum dots grown by molecular beam epitaxy are discussed, followed by results for the quantum dot detectors and emitters that have been developed at the University of Michigan, Ann Arbor.

Keywords: Self-organized quantum dots; infrared detectors; infrared sources; intersub-band devices.

1. Introduction

Two hundred years have passed since 1800, when Sir William Herschel first discovered infrared light. Since that time, infrared detection and emission have become cornerstones of the technological age. Infrared light is so appealing because it allows one to see when visible light does not. This so-called "night vision" is very familiar due to the frequent depiction of infrared imaging in popular culture, especially science fiction movies. However, infrared detectors and emitters are also crucial for an abundance of other applications. Infrared detectors are necessary for military targeting and tracking, law enforcement, medical diagnoses, space science, and even art. On the emitter side, there is an increasing demand for infrared sources for

Report Documentation Page				Form Approved OMB No. 0704-0188	
Public reporting burden for the collection of information is estimated to average 1 hour per response, including the time for reviewing instructions, searching existing data sources, gathering and maintaining the data needed, and completing and reviewing the collection of information. Send comments regarding this burden estimate or any other aspect of this collection of information, including suggestions for reducing this burden, to Washington Headquarters Services, Directorate for Information Operations and Reports, 1215 Jefferson Davis Highway, Suite 1204, Arlington VA 22202-4302. Respondents should be aware that notwithstanding any other provision of law, no person shall be subject to a penalty for failing to comply with a collection of information if it does not display a currently valid OMB control number.					
1. REPORT DATE 2002		2. REPORT TYPE		3. DATES COVERED 00-00-2002 to 00-00-2002	
4. TITLE AND SUBTITLE Quantum Dot Infrared Detectors and Sources				5a. CONTRACT NUMBER	
				5b. GRANT NUMBER	
				5c. PROGRAM ELEMENT NUMBER	
6. AUTHOR(S)				5d. PROJECT NUMBER	
				5e. TASK NUMBER	
				5f. WORK UNIT NUMBER	
7. PERFORMING ORGANIZATION NAME(S) AND ADDRESS(ES) University of New Mexico, Department of Electrical and Computer Engineering, Center for High Technology Materials, Albuquerque, NM, 87106				8. PERFORMING ORGANIZATION REPORT NUMBER	
9. SPONSORING/MONITORING AGENCY NAME(S) AND ADDRESS(ES)				10. SPONSOR/MONITOR'S ACRONYM(S)	
				11. SPONSOR/MONITOR'S REPORT NUMBER(S)	
12. DISTRIBUTION/AVAILABILITY STATEMENT Approved for public release; distribution unlimited					
13. SUPPLEMENTARY NOTES					
14. ABSTRACT					
15. SUBJECT TERMS					
16. SECURITY CLASSIFICATION OF:			17. LIMITATION OF ABSTRACT Same as Report (SAR)	18. NUMBER OF PAGES 26	19a. NAME OF RESPONSIBLE PERSON
a. REPORT unclassified	b. ABSTRACT unclassified	c. THIS PAGE unclassified			

optical IR spectroscopy, monitoring chemical species and pollutants, point-to-point atmospheric communication, remote controls, fiber optic telecommunication, and optical radars.

Infrared light is important for these various applications because of two main reasons. First of all, the blackbody radiant emittance for objects with a temperature less than or equal to 1000 K peaks in the infrared wavelength range. Another reason infrared light is so important is that due to its longer wavelength, it does not have the same scattering/absorption characteristics as visible light. The earth's atmosphere has transparent windows where infrared light is not significantly absorbed by the carbon dioxide and water that are present. These wavelength ranges are the mid-wavelength infrared (MWIR) from 3–5 μm , the long-wavelength infrared (LWIR) from 8–14 μm , and the far infrared (FIR) from 14–25 μm . These atmospheric windows make many of the infrared applications that are in use today possible.

Quantum dot devices, comprised of self-organized In(Ga)As/Ga(Al)As quantum dots, have recently demonstrated very promising results as infrared detectors^{1–18} and emitters.^{19–23} These devices offer several favorable attributes. In terms of infrared detection, quantum dot infrared photodetectors (QDIPs) are inherently sensitive to normally incident infrared light, they can potentially achieve high-temperature operation (> 100 K), and they have a low dark current.^{24,25} As for quantum dot infrared emitters, the advantages of high-temperature operation, low threshold current, and high modulation bandwidth associated with typical quantum dot interband lasers are still expected in these devices. In addition, the electron relaxation time from the higher energy states of the quantum dot to the ground state is such that intersubband lasing is possible by inducing a population inversion through interband spontaneous emission. The details of these advantages, as well as device fabrication and performance will be discussed later.

This chapter will review: (i) a brief history of infrared detection and emission, (ii) the optical and electrical characteristics of self-organized In(Ga)As/GaAs quantum dots grown by molecular beam epitaxy (MBE), (iii) results for the quantum dot detectors and emitters that have been developed at the University of Michigan, Ann Arbor, and finally, (iv) a projection for the future of these devices.

2. Historical Background

In 1800, Sir William Herschel discovered infrared light while conducting the following classic experiment. Sunlight was directed through a prism in order to obtain the visible spectrum of light. A thermometer was placed in the path of the different colors, and the temperature was measured as a function of energy (or light frequency). Much to his surprise, Herschel discovered that just outside of the spectrum, at a frequency below that of red, the thermometer measured the highest temperature, even though he could see no light. This newly discovered invisible light was called ultrared, and later infrared (or below-red) in 1870. During the 1800s, the development of the first thermal detectors of infrared radiation occurred. In

1830, a thermocouple was first used to measure radiant heat, and in 1880, the first bolometer was used to measure absorption in the earth's atmosphere. One hundred years after the discovery of infrared light, in 1900, Max Planck correctly described the radiant behavior of a blackbody. This significant accomplishment not only introduced the idea of quanta of energy, which eventually lead to the modern topic of quantum mechanics, but it also ushered in the era of microscopic science as opposed to macroscopic science. As a result, the 20th century is full of developments in light sources and semiconductor/solid state microelectronic devices. In addition to those mentioned above, a list of some significant scientific achievements related to infrared detection and emission can be found in Ref. 26.

There are two main classes of infrared detectors: thermal and photon detectors. Thermal detectors are made of materials whose physical properties change in the presence of radiant heat. The most common thermal detectors are: (i) thermocouples, which experience a change in voltage at the junction of two different solid state materials; (ii) bolometers, which experience a change in the resistance of bulk metal; and (iii) pyroelectric detectors, which experience a change in the surface charge of a material. Thermal detectors, which are readily available commercially, are less expensive than photon detectors, and they offer uncooled operation, which means that they are more portable for field applications. However, thermal detectors generally have a slower response to changing input, and they cannot offer two-color detection in a single device, a requirement for achieving high-resolution imaging. Thus photon detectors are often preferred for more sophisticated applications.

Photon detectors, which directly detect incident infrared radiation, can be either photoconductive (generate a corresponding photocurrent) or photovoltaic (generate a corresponding photovoltage). Photon detectors are usually made of semiconductor materials, be it three-dimensional bulk material (like HgCdTe), semiconductor heterostructures (like Type II InSb superlattices), or low-dimensional heterostructures (like III-V quantum well- and quantum dot-infrared photodetectors). All photon detection technologies are limited in that the detecting element must be cooled, which means that a dewar, cryostat, or thermoelectric cooler of some type is required. Photon detectors must be cooled in this way because the energy corresponding to infrared light is so small that the dark current generated at higher temperatures easily drowns any real signal created by the detector. The advantages and disadvantages of three types of photon detectors; mercury cadmium telluride detectors,²⁷⁻²⁹ quantum well infrared photodetectors,³⁰⁻³³ and quantum dot infrared photodetectors,¹⁻¹⁸ are discussed below.

Mercury cadmium telluride (MCT) detectors are intrinsic, bulk material detectors, which means they detect IR light corresponding to the energy gap of the semiconductor. MCT detectors are the industry standard, used in most state-of-the-art infrared imaging cameras in the MWIR and LWIR ranges. However, there are some drawbacks to this technology. First, there are difficulties in growing MCT, such as the requirement for effusion cell temperature feedback/control during growth for consistent material composition. Moreover, MCT experiences nonuniform dopant

incorporation, which leads to variations in device responsivity, adversely affecting the pixel operability of large area focal plane arrays. Another disadvantage, due to Auger recombination processes that severely reduce photoexcited carrier lifetimes, is that the MCT detector requires an operating temperature less than or equal to 80 K.²⁸

The GaAs/AlGaAs quantum well infrared photodetector (QWIP) is an alternative technology that detects infrared (IR) light through intersubband transitions in the conduction band. The required operating temperature for QWIPs (≤ 60 K) is lower than for MCT detectors because thermionic emission in MCT, for equivalent device parameters, is approximately five orders of magnitude less than in a QWIP.^{28,33} The QWIP benefits from mature III-V growth and processing techniques. QWIPs are also extremely uniform across a large area, which increases the pixel operability in a focal plane array. However, QWIPs require the fabrication of random reflectors at the top of detector pixels in order to allow lateral incidence since they cannot detect normally incident light due to polarization selection rules.³⁰

In(Ga)As/Ga(Al)As quantum dot infrared photodetectors (QDIPs), which also detect light through intersubband transitions in the conduction band, as shown in Fig. 1, benefit from the same advantages as the QWIP in terms of III-V growth and processing. In addition, there are three main advantages of the QDIP: normal-incidence detection, high-temperature operation, and low dark current. The polarization selection rules corresponding to three-dimensional electron confinement in quantum dots allow QDIPs to detect normally incident light.^{5,9,13} High-temperature operation in QDIPs results from a large electron relaxation time from the higher energy states of the quantum dot to the ground state. As a result, photoexcited carriers that escape from the dot have a higher probability of contributing to the photocurrent before relaxing back into the ground state.^{11,24} Thus, these increased relaxation times can lead to improved responsivity of the QDIP, which in turn allows higher operating temperatures. QDIPs are also

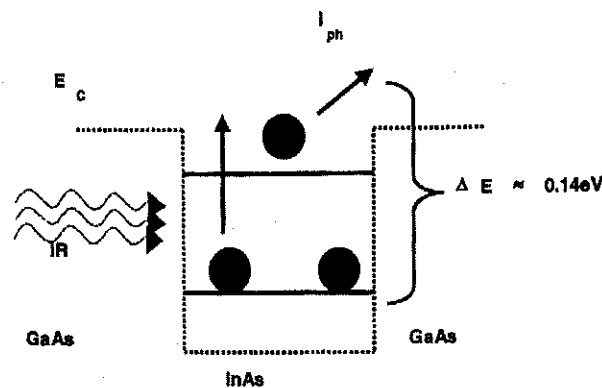


Fig. 1. Intersubband transition within the conduction band of an InAs/GaAs quantum dot for IR detection.

theoretically predicted to have lower dark currents than MCT detectors and QWIPs.²⁵ This is predicted because the three-dimensional quantum confinement of the electron wave function leads to the equality of the photoionization energy and the activation energy of thermionic emission in quantum dots. The main disadvantage of the QDIP is the random variation of dot size, shape, and composition due to the Stranski-Krastanow growth mode. As a result, the uniformity of quantum dots across a large area is reduced. Another growth-related issue is that nonuniform dopant incorporation adversely affects the responsivity of the QDIP, as in the MCT detector.

As far as infrared emission is concerned, the most abundant source of infrared light is the sun. However, sunlight is not a convenient source for laboratory experiments and practical applications. Instead, blackbody sources such as the Nernst glower (typically made from zirconia, yttria, or thoria) and the globalar (made from silicon carbide) are often used. These sources usually emit light from the visible range to the far infrared ($\approx 30 \mu\text{m}$). Two other important sources of infrared light are solid-state light emitting diodes (LEDs) and lasers. While there are many types of LEDs and lasers that emit light in the near-infrared (from 0.9 to $2 \mu\text{m}$), there are very few that emit light in the MWIR, LWIR, and FIR ranges. Due to the small energy spacing that corresponds to infrared light in the desired range, bulk material is usually not suitable for such devices. Instead, there is a heavy dependence on quantum well and quantum dot devices, which are relatively new developments, especially when compared to the long history of infrared detection.

Early reports on light emitting diodes³⁴⁻³⁶ were followed by an account of the quantum cascade laser,³⁷⁻³⁹ a novel unipolar semiconductor laser based on intersubband transitions in quantum wells. MIR emission has also been reported in quasi one-dimensional wires grown by molecular beam epitaxy (MBE) and in optically pumped quantum fountain lasers.^{40,41} Recently, room temperature photoluminescence has been reported in the 3-4 μm range using PbSe/PbSrSe multiple quantum well structures.⁴² Self-organized quantum dots are expected to display MIR emission and absorption characteristics as the energy spacing of the bound states in these dots lies in the MIR regime. Vorob'ev *et al.* have reported the observation of weak MIR emissions from interband InGaAs/GaAs quantum well and InGaAs/AlGaAs quantum dot lasers.¹⁹ More recently, Krishna *et al.*²⁰⁻²² and Grundmann *et al.*,²³ have reported mid-infrared emission (12 and 16 μm) from near-infrared quantum dot lasers.

3. Self-Organized Quantum Dots for Devices

The realization of a high density of small ($\approx 100\text{-}200 \text{ \AA}$) and uniform quantum dots (QDs) has been elusive. The most direct approach, that is, epitaxial growth of a quantum well followed by controlled etching, provides the requisite size and uniformity. However, surface defects produced by the etching process reduce the radiative efficiency to levels that are not suitable for lasers, or other types of quan-

tum dot devices.⁴³ Recently, self-organized quantum dots have proven to be the structures which best approach desired device properties.⁴⁴⁻⁴⁶ The use of strain to produce self-assembled quantum dot structures is now a well-accepted approach and is widely used in III-V semiconductors and other material systems. Much progress has been made in the area of growth,⁴⁷⁻⁵⁰ where the focus has been size control, as well as optical characterization,⁵¹⁻⁵⁹ where the focus has been application to quantum dot detectors, sources, and other types of optoelectronic devices.

The use of defect-free strain-induced self-organized quantum dots provides several advantages. Due to the pyramidal shape of these dots and the complicated strain tensor with a strong hydrostatic component within them, large modulation of the interband photon energy can be produced. For example, InAs/GaAs quantum dot lasers emit at $\approx 1 \mu\text{m}$, a wavelength much smaller than that corresponding to the bandgap. Thus, another means of tunability is introduced.

It has been shown that highly lattice-mismatched In(Ga)As epitaxially grows on GaAs in the so-called Stranski-Krastanow growth mode, where self-organized islands are formed after a few monolayers of layer-by-layer growth.⁶⁰ From RHEED measurements during molecular beam epitaxy (MBE) of InGaAs on GaAs and from energy minimization considerations in a unit cell of the growing layer, it has been determined that for a misfit $f > 1.8\%$, the island mode of growth is preferred.⁶¹ For typical growth parameters used in MBE or metal-organic vapor phase epitaxy (MOVPE), an array of pyramidal islands of widths from 10–40 nm and heights from 5–8 nm are formed. Elastic relaxation on the facet edges, renormalization of the surface energy of the facets, and interaction between neighboring islands via the substrate are the driving forces for self-organized growth. As will be described later, there are considerable strain fields within the pyramidal dots, in the substrate underneath, and in the overlayer, if the latter is grown. *In situ* atomic force microscopy (AFM) studies during growth of InAs on GaAs have given valuable insights into the evolution of the size distribution between dots, as growth proceeds, and a tendency for eventual size equalization.⁴⁸ Careful studies of growth in the InAs-GaAs system have also shown that there exists a relatively narrow range of deposition parameters where the islands are small ($\approx 10 \text{ nm}$), have very similar size and shape, and form dense arrays.⁴⁵ Interaction of the islands via the substrate also makes their lateral ordering favorable.⁶² By virtue of their size and shape, the self-organized islands best approach the desired properties of zero-dimensional quantum dots. An AFM image of an array of $\text{In}_{0.4}\text{Ga}_{0.6}\text{As}/\text{GaAs}$ dots grown by MBE at 540°C and a rate of 0.25 monolayers/sec is shown in Fig. 2(a). From this image, the dot density is estimated to be $5 \times 10^{10} \text{ cm}^{-2}$. The pyramids have a base diagonal of 20 nm and a height of 7 nm. The cross-sectional transmission electron microscope (TEM) image of a single InAs dot grown by MBE at 500°C is shown in Fig. 2(b).

If a layer of InGaAs dots is covered with a thin layer of GaAs and another InGaAs growth cycle is initiated, the dots in the second sheet are formed exactly on top of the dots in the first layer and this trend continues, resulting in a 3D array of

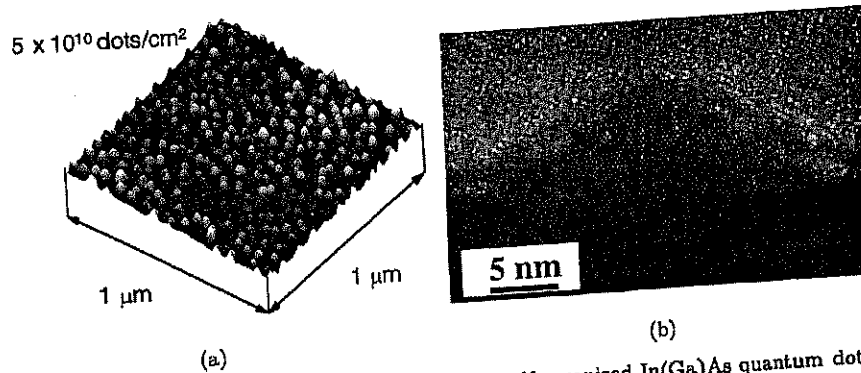


Fig. 2. (a) AFM image of a single layer of exposed self-organized In(Ga)As quantum dots. Dot density estimated from this image is $5 \times 10^{10} \text{ cm}^{-2}$; and (b) cross-sectional TEM image of a single InAs quantum dot.

vertically aligned and electronically coupled dots.^{63,64} Such multiple layer quantum dots (MLQDs) are very useful for device applications. The optimum growth conditions for multilayer dots have been described in detail previously.^{58,59} Some salient features, relevant to detector and emitter operation, are reiterated here. Usually, a smaller thickness of InGaAs needs to be deposited for subsequent quantum dot layers. This is because the wetting layer thickness progressively decreases. For example, in the case of $\text{In}_{0.4}\text{Ga}_{0.6}\text{As}/\text{GaAs}$ quantum dots, seven monolayers (MLs) of InGaAs need to be deposited for the first dot layer, and subsequent dot layers are formed with 3–5 MLs of InGaAs, depending on the GaAs barrier layer thickness.

4. Electronic Spectra and Carrier Dynamics in Self-Organized Quantum Dots

Bandstructure calculations of individual $\text{In}_{0.4}\text{Ga}_{0.6}\text{As}/\text{GaAs}$ quantum dots based on an eight-band, $\mathbf{k} \cdot \mathbf{p}$ formalism, including the strain distribution in the dots, predicts the bandstructure shown in Fig. 3.⁶⁵ There are two electron levels and several hole levels confined in the dots. In real quantum dot ensembles, these discrete levels are inhomogeneously broadened due to the size variation of the dots. In addition, level splittings occur due to interdot coupling, causing the formation of bands of electronic levels around the central excited- and ground-state levels. The excited level in each dot has a two-fold degeneracy due to the symmetry of the dot geometry. In the four vertically coupled dot configuration, the excited levels form a band of eight levels each of which has a spin degeneracy of two. The ground state band consists of four levels, each with a spin degeneracy of two. Photoluminescence data depicting the ground state and excited state transitions in $\text{In}_{0.4}\text{Ga}_{0.6}\text{As}/\text{GaAs}$ dots are shown in Fig. 4. There are higher order electron states in dots with different compositions. Hence, the electron interband, as well as intersubband, energies can greatly vary with dot size, dot composition, and the heterostructure band offsets.

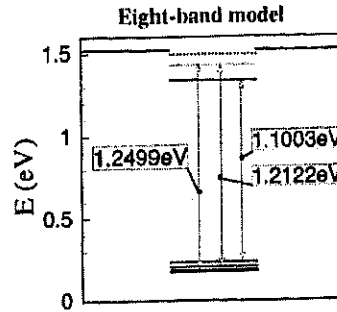


Fig. 3. Theoretical eight-band, $k \cdot p$ bandstructure of a single $\text{In}_{0.4}\text{Ga}_{0.6}\text{As}/\text{GaAs}$ quantum dot.

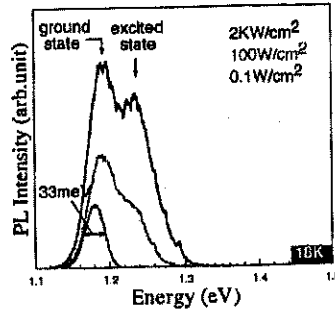


Fig. 4. Photoluminescence measurements of $\text{In}_{0.4}\text{Ga}_{0.6}\text{As}/\text{GaAs}$ quantum dots. Excited state transitions are visible in addition to ground state transitions with increasing excitation intensity. The curves of largest, median, and smallest areas correspond to $2 \text{ KW}/\text{cm}^2$, $100 \text{ W}/\text{cm}^2$ and $0.1 \text{ W}/\text{cm}^2$, respectively.

Femtosecond pump-probe differential transmission spectroscopy (DTS) measurements have been performed on four-layer $\text{In}_{0.4}\text{Ga}_{0.6}\text{As}/\text{GaAs}$ quantum dot heterostructures at temperatures $\geq 10 \text{ K}$ for a range of excitation levels.^{66,67} Electron-hole pairs are generated in the barrier region of the dots using a 100 fs, 800 nm pump beam. The DTS signal at the ground and excited state transition energies are then measured as a function of the delay between the pump and probe pulses. Since the DTS signal is proportional to the occupation number of each level, the relaxation times are obtained directly using this technique.

In terms of QDIP operation, the results from the DTS measurements suggest that at temperatures of 77 K and higher, there is a significant electron lifetime (\approx hundreds of picoseconds) in the higher-lying states. With an applied transverse bias, the lifetime can become even larger. When IR photons are absorbed by the QDIP, electrons are excited to the higher-lying states directly, or they are raised to the dot excited states, from where they are emitted to the higher-lying states. The probability of these electrons (which contribute to the photocurrent) relaxing back into the ground state is small, particularly at high temperatures. It is important

to realize that the increased lifetime of electrons in the higher-lying states does not reduce the dark current in the same way increased carrier lifetime does in small bandgap junction IR detectors; however, photocurrent and responsivity are favorably impacted.

5. Quantum Dot Infrared Detectors and Focal Plane Arrays

The lateral QDIP and the vertical QDIP are two general device structures that have been studied. The lateral QDIP, which operates much like a field-effect-transistor, conducts photocurrent through lateral transport of carriers across a high-mobility channel. AlGaAs barriers, which provide this high-mobility channel, are also necessary to modulation-dope the quantum dots. Since the major contributions to the dark current in lateral QDIPs are due to interdot tunneling and hopping conduction, these devices have demonstrated lower dark currents and higher operating temperatures than vertical QDIPs.¹² The vertical QDIP conducts photocurrent through vertical transport of carriers. In this case, the quantum dots are directly doped to provide free carriers during photoexcitation, and an AlGaAs barrier can be included in the vertical device to block dark current created by thermionic emission.¹⁶ Both types of devices can be grown by solid source molecular beam epitaxy (MBE) or metal-organic vapor phase epitaxy (MOVPE). Typical MBE growth conditions for both devices are related below.

For the lateral QDIP, a 1 μm GaAs buffer layer is grown at 620°C on a semi-insulating (100) GaAs substrate, followed by a 300 Å $\text{Al}_{0.18}\text{Ga}_{0.82}\text{As}$ barrier, which forms a high-mobility channel with the subsequent 500 Å GaAs spacer layer. The 18% AlGaAs layer is silicon-doped ($n = 1 \times 10^{17} \text{ cm}^{-3}$) in order to provide free carriers to the quantum dots by modulation-doping. Next, the substrate temperature is decreased to 500°C, and 2.2 ML of InAs are deposited to form the quantum dots. A 500 Å GaAs cap layer is then grown over the dots, and this sequence is repeated nine times for a total of ten InAs/GaAs quantum dot layers bordered by an 18% AlGaAs layer on either side. After the final 18% AlGaAs barrier deposition, a silicon-doped ($n = 2 \times 10^{18} \text{ cm}^{-3}$) GaAs contact layer is grown for the two top metal contacts of the device. The device heterostructure is shown in Fig. 5(a).

For the vertical QDIP, a 0.5 μm silicon-doped ($n = 2 \times 10^{18} \text{ cm}^{-3}$) GaAs contact layer is deposited on a semi-insulating (100) GaAs substrate at 620°C, followed by a 250 Å intrinsic GaAs buffer layer. The substrate temperature is decreased to 500°C, and 2.2 ML of InAs are deposited to form the directly-doped quantum dots ($n = 1 \times 10^{18} \text{ cm}^{-3}$). A 250 Å intrinsic GaAs cap layer is grown on top of the InAs in order to complete the quantum dot barrier. This sequence of growth is then repeated nine times for a ten-layer InAs/GaAs quantum dot active region. After the final GaAs layer is grown, the substrate temperature is increased to 620°C, and 400 Å of intrinsic $\text{Al}_{0.3}\text{Ga}_{0.7}\text{As}$ are deposited in order to form a current-blocking barrier at the top of the device. Finally, a 0.1 μm silicon-doped ($n = 2 \times 10^{18} \text{ cm}^{-3}$) GaAs top contact layer is grown, as shown in the device heterostructure in Fig. 5(b).

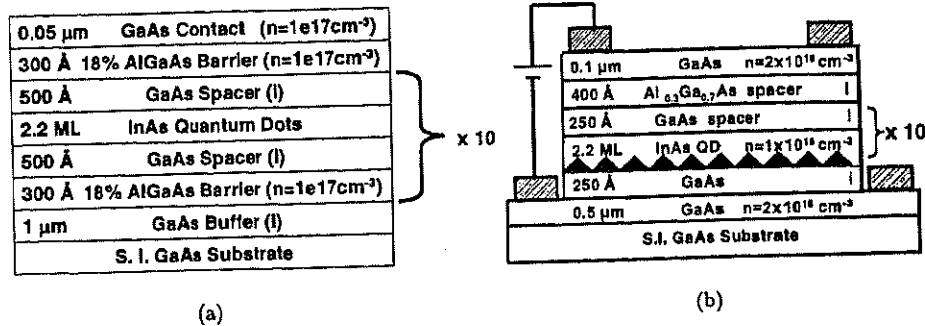


Fig. 5. Molecular beam epitaxy heterostructures for (a) a modulation-doped lateral QDIP and (b) a directly-doped vertical QDIP.

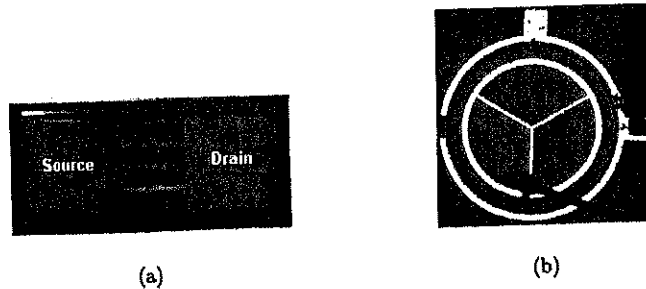


Fig. 6. SEM micrograph of fabricated device for (a) a lateral QDIP with optical area $8.4 \times 10^3 \mu\text{m}^2$ and (b) a vertical QDIP with optical area $2.83 \times 10^5 \mu\text{m}^2$.

The lateral and vertical QDIPs are then fabricated using standard photolithography and wet-etching techniques. The lateral QDIP requires a two-step process. First, the two top Ni/Ge/Au/Ti/Au metal contacts with interdigitated fingers are evaporated, followed by a recess etch in order to prevent shorting of the device. Second, a mesa etch is performed in order to define the active region of the device. The vertical QDIP requires a three-step process. The first step comprises metal evaporation for the top ring contact. Second, a mesa etch ($\approx 1 \mu\text{m}$) around the top contact defines the active region. Third, the metal evaporation is repeated for the bottom ring contact around the device mesa. Ohmic contacts are achieved in both devices by annealing at 400°C for approximately one minute. The fabricated lateral and vertical devices are shown in Figs. 6(a) and 6(b), respectively.

While there are performance advantages in using lateral QDIPs, it will be very difficult to fabricate these devices as focal plane arrays since each pixel requires three contacts (or three bump bonds), two for the top lateral contacts and one for a common ground. Therefore, it is necessary to improve the performance of the vertical QDIP since it is much more compatible with commercially available read-out circuits. In the remainder of this section, the performance of a vertical InAs/GaAs QDIP with a current-blocking $\text{Al}_{0.3}\text{Ga}_{0.7}\text{As}$ barrier is examined.

Dark current, spectral response, and blackbody response measurements are conducted in order to characterize the vertical QDIP. Typical dark current-voltage characteristics are shown in Fig. 7 for a range of temperatures from 78 K to 295 K. The dark current of this QDIP ($I_{\text{dark}} = 1.7 \text{ pA}$, $V_{\text{bias}} = 0.1 \text{ V}$, $T = 100 \text{ K}$) is much lower than that measured in a similar $\text{In}_{0.15}\text{Ga}_{0.85}\text{As}/\text{GaAs}$ QWIP device ($I_{\text{dark}} = 10 \text{ } \mu\text{A}$, $V_{\text{bias}} = 0.1 \text{ V}$, $T = 60 \text{ K}$).³¹ This reduction in dark current is due to the AlGaAs barrier at the top of the device heterostructure. The asymmetry in the I-V curves is also due to the AlGaAs barrier in that it only blocks current near the top contact. The activation energy (E_a), determined by considering the linear sections of the Arrhenius plots of the dark current, is shown as a function of bias in Fig. 8. The asymmetry of the activation energy is also a direct result of

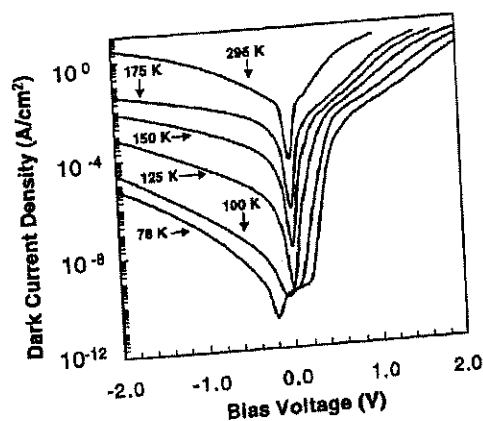


Fig. 7. Dark current-voltage characteristics for temperature range from 78 K to 295 K.

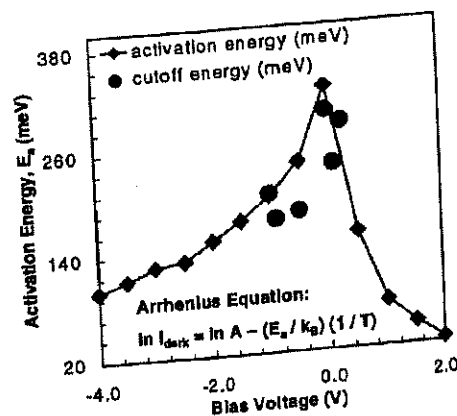


Fig. 8. Activation energy, E_a (♦), as a function of bias voltage, as calculated from Arrhenius plots. The calculated activation energies show reasonably good agreement with the measured cutoff energies (●) of the spectral response for several bias voltages.

the asymmetry in the heterostructure. As shown in Fig. 8, these activation energies agree with the cutoff energies measured in the spectral response of the detector, which is discussed next.

A Fourier Transform Infrared (FTIR) spectrometer with a broadband (1 to 20 μm), high intensity source is used to determine the spectral response of the QDIP at normal-incidence. The spectral response is obtained for a detector temperature of 78 K and a bias range from -1.0 V to 0.25 V. Figure 9(a) depicts the spectral response at a bias of 0.1 V. The peak wavelength, λ_{peak} , is 3.72 μm , and the linewidth, $\Delta\lambda/\lambda$, is 0.3, most likely a bound-to-continuum intersubband transition.⁵ The spectral characteristics (λ_{peak} and $\Delta\lambda/\lambda$) of the vertical QDIP change with bias, as shown in Fig. 9(b). As the bias becomes less negative, λ_{peak} blue-shifts to shorter wavelengths and $\Delta\lambda/\lambda$ decreases. The blue-shift of the peak wavelength is due to the decrease in band bending of the conduction band as the bias voltage nears zero volts. The significant decrease in $\Delta\lambda/\lambda$ is not a function of device operation, but rather results from the strong atmospheric absorption that occurs below 3 μm .

The blackbody response of the vertical QDIP is measured as a function of detector temperature and bias voltage. A calibrated, 800 K blackbody source is used to determine the absolute responsivity of the QDIP to normally incident IR radiation, and a germanium block is used to filter out near-IR radiation ($< 1.8 \mu\text{m}$) emitted by the blackbody. The QDIP photocurrent signal and noise are measured with a Fast Fourier Transform (FFT) Analyzer. A flat-band noise spectrum is desired because it indicates that the dominant noise mechanism is generation-recombination (GR) noise, as assumed in most theoretical calculations. The QDIP is characterized at 78 K, 100 K, 125 K, and 150 K. For temperatures greater than 150 K, the signal-to-noise ratio measured by the FFT analyzer is less than one. The best

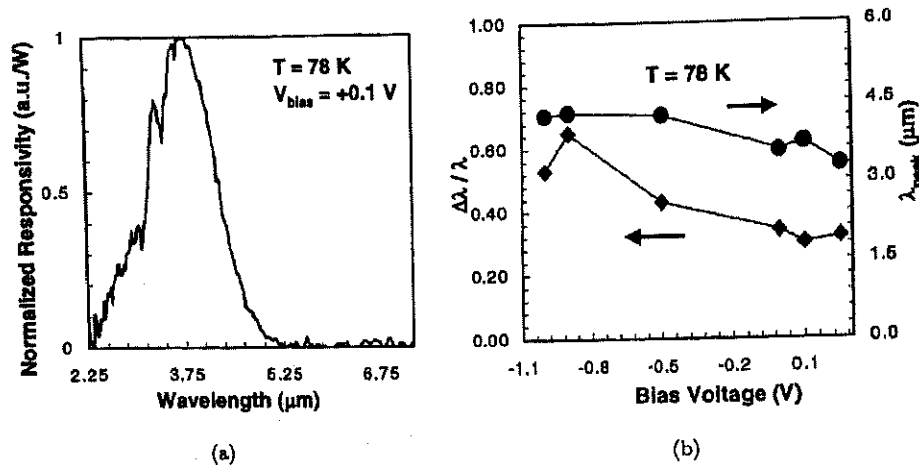


Fig. 9. Relative spectral response of vertical QDIP at a bias of 0.1 V and temperature of 78 K and (b) bias voltage dependence of the peak wavelength, λ_{peak} , and the FWHM linewidth, $\Delta\lambda/\lambda$, at 78 K.

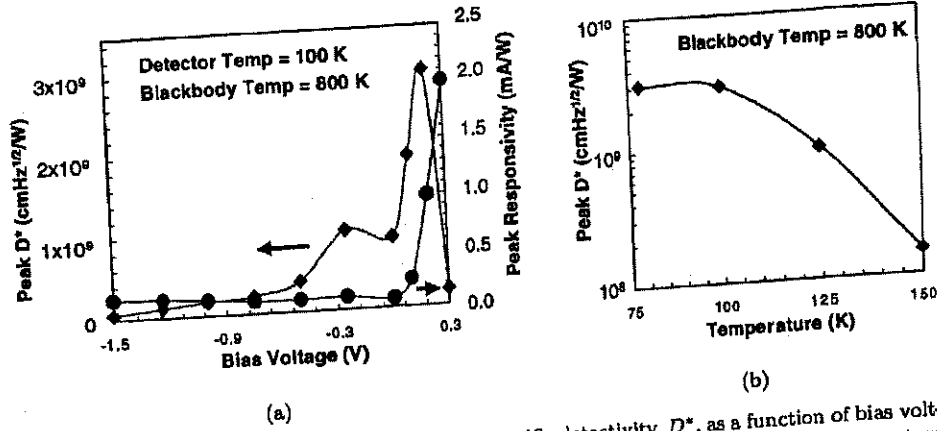


Fig. 10. (a) Peak responsivity, R_{peak} , and peak specific detectivity, D^* , as a function of bias voltage calibrated by an 800 K blackbody at a temperature of 100 K; and (b) the detector temperature dependence of D^* .

device performance is measured at 100 K, and the bias-dependent R_{peak} and D^* values for the device at this temperature are shown in Fig. 10(a). The responsivity, and therefore, the detectivity are relatively low at negative biases because the AlGaAs barrier prevents carriers from being collected at the contact under reverse bias. Even the maximum R_{peak} value, 2 mA/W for a bias of 0.3 V at 100 K, is low because of the AlGaAs barrier, which blocks photocurrent as well as dark current. The responsivity quickly increases for positive biases, however, and at a low forward bias, a large D^* can be obtained before the dark current increases and drives down the signal-to-noise ratio. A maximum D^* of 2.94×10^9 cmHz^{1/2}/W at a bias of 0.2 V is obtained at 100 K, and this is a significant milestone in the performance of normal-incidence, vertical QDIPs. The temperature dependence of the maximum D^* values is shown in Fig. 10(b).

Since the blackbody response measurement does not consider the wavelength of IR light that is detected, the peak values R_{peak} and D^* shown in Fig. 10 are calculated using a blackbody-to-peak conversion factor. This conversion factor, Γ , which is inversely proportional to the relative response (per watt) measured by the spectral response, multiplies both the responsivity and detectivity calculated from the signal and noise values obtained during the blackbody response measurement:

$$R_{\text{peak}} = \Gamma \times \frac{I_{\text{photo}}}{P_{\text{incident}}}, \quad (1)$$

$$D^* = \Gamma \times \frac{I_{\text{photo}}}{P_{\text{incident}}} \times \frac{(A_{\text{detector}} \Delta f_{\text{noise}})^{1/2}}{I_{\text{noise}}}, \quad (2)$$

where I_{photo} is the measured photocurrent, P_{incident} is the photon power incident on the detector determined from the blackbody calibration, A_{detector} is the approximate optical area of the device, Δf_{noise} is the bandwidth over which the noise

voltage is measured, and I_{noise} is the measured noise current. Another important quantity that must be calculated is the photoconductive gain in the quantum dot detector. The gain mechanism in these vertical QDIPs is due to the increased carrier relaxation times in the excited states of quantum dots, which decrease the capture probability of free carriers in quantum dots.^{11,24} The photoconductive gain for a QWIP can be expressed in terms of the capture probability by^{11,68,69}:

$$g = \frac{1}{Np(1+p)}, \quad (3)$$

where p is the capture probability ($p \ll 1$) and N is the number of quantum well layers. This equation is approximately correct for quantum dots after including an additional fill factor, F , in the denominator that takes into account the surface density of discrete dots across a single epitaxial layer. Since the capture probability in quantum dots is very small, the gain in QDIPs is greater than one, with expected values in the range from 1–5.¹¹ Figure 11 shows the bias dependence of the photoconductive gain at a detector temperature of 100 K.

Ultimately, it is of interest to incorporate QDIPs in focal plane arrays (FPAs). In order to make a preliminary assessment of the uniformity of the dots and device processing, the room temperature dark current of the devices in an individually addressed (4×4) array are measured. The result is shown in Fig. 12(a). It is apparent that the dark current is fairly constant across this small array (for 0.1 V bias, the standard deviation, σ , is 3.07×10^{-5}) despite the large nonuniformity that is characteristic of the Stranski–Krastanow growth mode. However, it is obvious that FPAs will involve larger areas on the grown wafer.

An attempt to demonstrate imaging with QDIPs, using a raster-scan imaging system where the field-of-view is scanned simultaneously in the x - and y -axes by two mirrors, is described below. An array of photocurrent/voltage values is compiled as the field-of-view is scanned, either by a single detector or a small, interconnected detector array. In this way, infrared imaging is demonstrated with self-organized InAs/GaAs quantum dot infrared photodetectors.

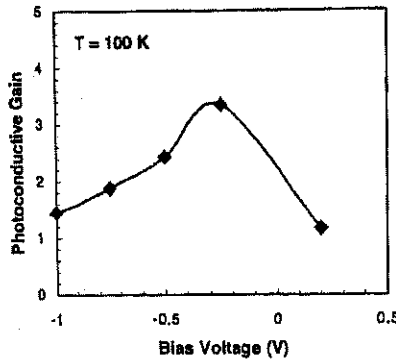


Fig. 11. Photoconductive gain as a function of bias voltage for a detector temperature of 100 K.

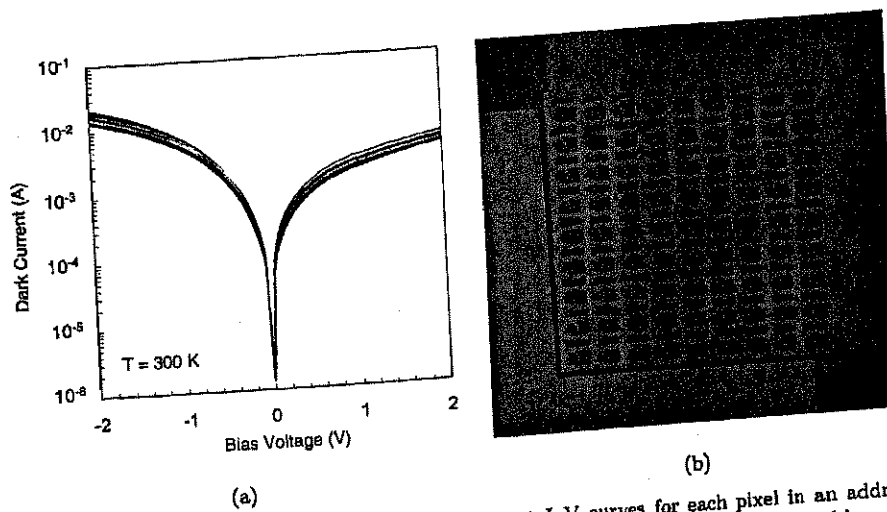


Fig. 12. (a) Room temperature (300 K) dark current I-V curves for each pixel in an addressable 4×4 QDIP array; and (b) SEM micrograph of a (9×9) interconnected, nonaddressable InAs/GaAs QDIP array with $40 \mu\text{m}$ mesa size and $120 \mu\text{m}$ pitch.

While raster-scan imaging should work with a single detector, a small array is actually used because it is easier to collect infrared light over a larger area. Also, the average photocurrent from an array should be larger, and therefore, much easier to distinguish from background noise. Standard photolithography and wet-etch processing are used to fabricate (4×4) , (9×9) , and (13×13) individually addressable and nonaddressable (interconnected) arrays of vertical, mesa-shaped QDIPs. The pixel diameter is $40 \mu\text{m}$, and the array pitch is $120 \mu\text{m}$. The photomicrograph of an interconnected, (9×9) QDIP array is shown in Fig. 12(b). The entire array effectively behaves as a single detector with a very large optical area and a single photocurrent signal.

Examples of images obtained by the vertical QDIP array through this raster-scan technique are shown in Fig. 13. Figure 13(a) shows the image of a 20 W

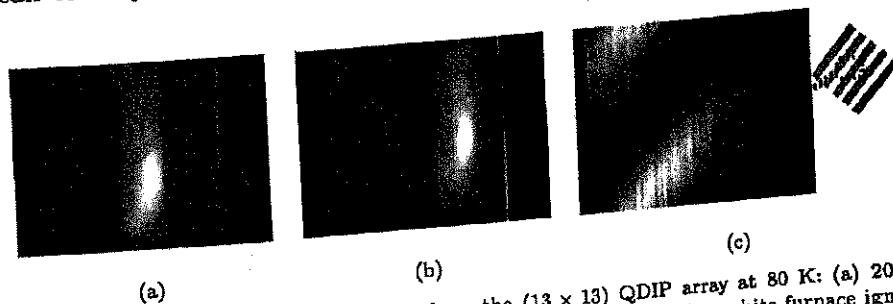


Fig. 13. Raster-scanned images obtained from the (13×13) QDIP array at 80 K: (a) 20 W broadband infrared globar source through a circular pinhole, (b) heated graphite furnace igniter through a circular hole and linear slit, and (c) heating element from a hot plate, shown schematically in the inset, partially showing two metal strips.

broadband infrared globar source through a circular pinhole. Figure 13(b) is the image of a 700°C furnace igniter shielded by an aluminum block with a circular pinhole and a linear slit. Figure 13(c) depicts the partial image, in this case limited by the field-of-view of the scanning mirrors, of the heating element of a hot plate at 500°C. Portions of the heated strips (schematically shown in the inset) are seen as the bright regions. These results indicate that, in spite of the low responsivity of the QDIPs, they can be used for imaging. With progressive improvement of device performance, they should be applicable to focal plane arrays.

6. Quantum Dot Infrared Sources

The electron energy level spacing between (i) the ground state and the first excited state and (ii) the ground state and the GaAs conduction band edge in $\text{In}_{0.4}\text{Ga}_{0.6}\text{As}/\text{GaAs}$ self-organized quantum dots are about 60–80 meV and 230–250 meV, respectively, as determined from theory and experiments.^{59,65} From analysis of the small-signal modulation of quantum dot interband lasers, electron relaxation times from higher-energy states to the ground state at room temperature have been estimated to be as long as 30–50 ps.²⁴ This is supported by DTS measurements,^{66,67} as described in Sec. 4. These favorable relaxation times invoke the possibility of intersubband lasing in quantum dots. This was first suggested by Singh, who proposed the use of an external interband laser to rapidly depopulate the ground state electrons by stimulated emission, thus creating a favorable nonequilibrium carrier distribution between the ground and excited states for MIR emission.⁷⁰ Recently, Kastalsky *et al.*, have theoretically analyzed a similar dual-color laser using a three-level carrier rate equation.⁷¹ Also, Krishna *et al.* recently demonstrated intersubband stimulated emission in interband quantum dot lasers.²²

For population inversion to occur, the energy relaxation time between the upper level excited states and the ground state, τ_{u1} , should be as long as possible, and the lifetime of electrons in the ground states, τ_1 , should be very short. Providing a high density of coherent photons in the cavity, which can greatly reduce the interband electron-hole recombination time, τ_{stim} , can decrease the lifetime of the electron in the ground state. A high density of coherent photons can be made available in the intersubband laser cavity by simultaneous interband lasing due to current injection.

In order to examine population inversion between the ground state and the excited dot states, the following rate equations are solved self-consistently:

$$\begin{aligned} \frac{dn_u}{dt} = & \eta_{in} \frac{J}{e} - \frac{n_u g_u (1 - f_l)}{\tau_{u1}} + \frac{n_l g_l (1 - f_u)}{\tau_{lu}} - \frac{n_u g_u f_u f_h}{\tau_u} \\ & + \frac{n_{phu} n_u g_u (1 - f_u - f_h)}{\tau_u} = 0, \end{aligned} \quad (4)$$

$$\begin{aligned} \frac{dn_1}{dt} = & (1 - \eta_{in}) \frac{J}{e} + \frac{n_u g_u (1 - f_1)}{\tau_{u1}} - \frac{n_1 g_1 (1 - f_u)}{\tau_{1u}} - \frac{n_1 g_1 f_1 f_h}{\tau_1} \\ & + \frac{n_{ph1} n_1 g_1 (1 - f_1 - f_h)}{\tau_1} = 0, \end{aligned} \quad (5)$$

where η_{in} is the injection efficiency; n_{ph1} and n_{phu} are the photon occupation number of the ground state and the upper level excited states that are involved in the lasing process, respectively; n_1 and n_u are the density of ground states and excited states, respectively; and f_1 and f_u are the occupational probabilities of the ground state and excited states, respectively. The degeneracy of the ground state ($g_1 = 2$) and the excited states ($g_u = 4$)⁶⁵ are taken into account in the rate equation calculations. Interband recombination times for the ground state, τ_1 (= 700 ps) and the excited state, τ_u (= 250 ps) have been derived from time-resolved photoluminescence measurements,⁵⁹ and an intersubband relaxation time of $\tau_{u1} = 60$ ps is assumed. A thermal distribution of holes is used ($f_h = 0.45$). When the ground state photon occupation number is zero, $f_1 > f_u$ for all values of the injection current, and no population inversion is possible. However, when the ground state photon occupation number is increased to 50, f_1 is pinned at a value of ~ 0.5 , whereas f_u increases linearly with the current. Again, when the number of photons in the excited state (n_{phu}) is increased to 50, $f_1 > f_u$ for all values of injection. This is consistent with the fact that if $n_{phu} = 50$, interband lasing occurs from the excited state in the dot and no MIR emission results.

The overlap integral and the intersubband gain are calculated for various injection levels in accordance with the equation below^{72,73}:

$$g(\hbar\omega) = \frac{\pi e^2 \hbar |p_{12}|^2}{m_0^2 c n_r \epsilon_0 \hbar \omega} \frac{1}{\sqrt{1.44 \pi \sigma}} N_e \exp \left(-\frac{(\hbar\omega - E_{1u})^2}{1.44 \sigma^2} \right) [f(E_u^e) - f(E_1^e)]. \quad (6)$$

The results of the calculation are shown in Fig. 14. It is evident that gains up to 170 cm^{-1} can be achieved even if an inhomogeneous broadening of 20 meV is assumed for the interband transition. Nishi *et al.* have reported photoluminescence linewidths of 21 meV at room temperature.⁷⁴ The intersubband population inversion and lasing processes, together with the bipolar recombination, are illustrated in Fig. 15.

The results described here are performed on multi-dot layer, single-mode, ridge waveguide, interband lasers ($\lambda \sim 1 \text{ } \mu\text{m}$) grown by solid-source molecular beam epitaxy. The waveguide is designed for near-infrared emission. The gain region consists of a four dot-layer stack of $\text{In}_{0.4}\text{Ga}_{0.6}\text{As}$ dots, separated by 15 Å GaAs barriers in the middle of a GaAs waveguide and surrounded by 1 μm $\text{Al}_{0.3}\text{Ga}_{0.7}\text{As}$ outer cladding layers and appropriate GaAs contact layers.

Lasers are fabricated using standard photolithography, lift-off techniques, and a combination of dry and wet etching. The width of the waveguide is 3 μm , and the length of the laser varied from 400–600 μm . The output light is directed through a band pass filter, after which the light is coupled to a liquid nitrogen cooled MCT detector, which can detect radiation from 5–26 μm . Bandpass filters are used to

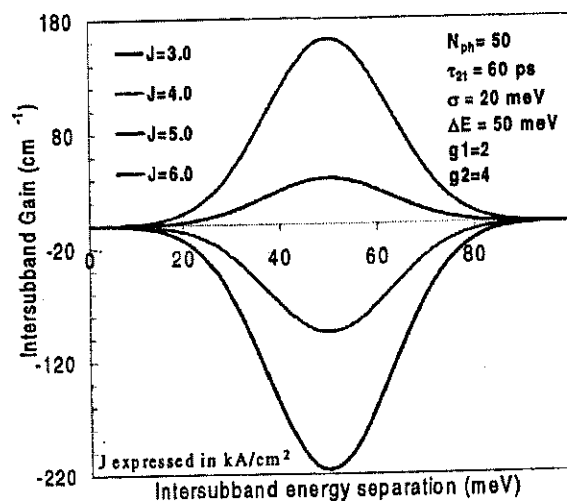


Fig. 14. Calculated intersubband gain in $\text{In}_{0.4}\text{Ga}_{0.6}\text{As}/\text{GaAs}$ quantum dots using a two-photon rate equation model. The curves with the larger positive gain, smaller positive gain, smaller negative gain, and larger negative gain correspond to $J = 6.0$, $J = 5.0$, $J = 4.0$, and $J = 3.0$, respectively.

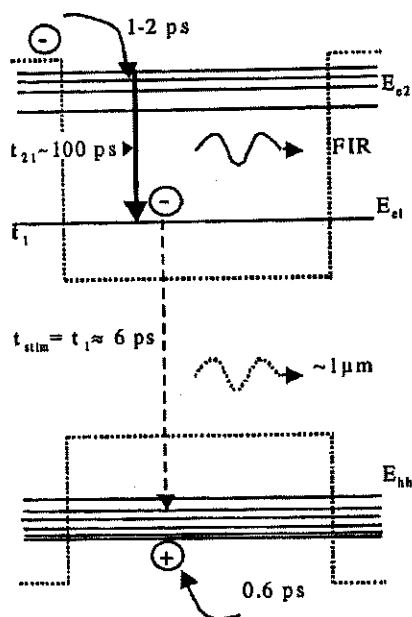


Fig. 15. Schematic illustration of electronic bound states, approximate carrier relaxation times and the intersubband population inversion process.

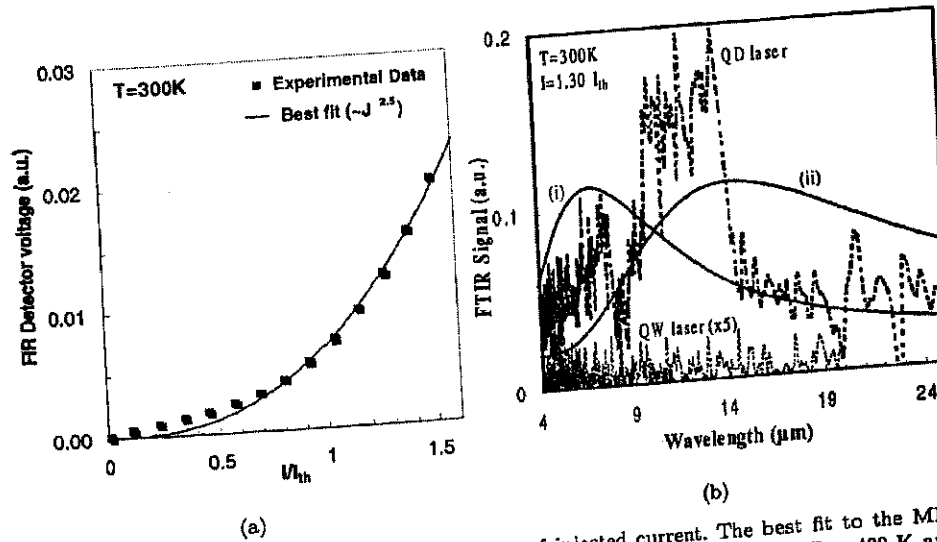


Fig. 16. (a) Spontaneous emission as a function of injected current. The best fit to the MIR emission ($J \propto I^\alpha$) is with $\alpha = 2.5$; and (b) radiation from a blackbody source at (i) $T = 420$ K and (ii) $T = 200$ K, corresponding to heat sink temperatures of 300 K and 80 K, respectively. The dotted line represents the room temperature FIR emission from the interband quantum dot laser at $I = 1.30I_{th}$.

select the MIR output. Figure 16(a) depicts the MIR signal amplitude as a function of injection current at $T = 17$ K and $T = 300$ K.

Spectral measurements of the MIR output are performed on the quantum dot lasers at $T = 80$ K and $T = 300$ K. The lasers are wire bonded and mounted in a cold finger cryostat with a ZnSe window and are biased with a low frequency positive pulse ($f = 10$ Hz, duty cycle = 25%). A silicon filter is used to block the interband signal at $1 \mu\text{m}$, and MIR emission is measured as a function of injection bias using an FTIR spectrometer. The recorded data is corrected for the ambient blackbody background response of the system. At $T = 300$ K, no emission is observed when the laser is biased below threshold. However as the threshold bias is reached, a broad peak attributed to intersubband transitions and centered around $12 \mu\text{m}$ is observed. This peak increases in amplitude until $I = 1.2I_{th}$, and then it remains almost constant in magnitude.

To confirm that the observed peaks are not due to thermal heating of the device, the data are analyzed by considering emission from a blackbody source. Local temperatures at the laser mirrors have been measured to be about 120°C higher than the temperature of the heat sink in GaAs-based quantum well lasers.⁷⁵ Using a value of $\Delta T = 120^\circ\text{C}$, the temperature of the laser mirrors is estimated to be about 420 K and 200 K when the heat sink is at 300 K and 80 K, respectively. The blackbody curves corresponding to these two temperatures are shown in Fig. 16(b), in addition to the observed room temperature spontaneous emission from the interband QD laser.

For the observation of stimulated intersubband emission, plasmon-enhanced waveguides are designed and grown by MBE. The confinement factor, Γ , for the intersubband mode is 3.7×10^{-4} . The waveguide loss, α_w , is calculated to be 6.84 cm^{-1} . The width of the waveguide varies from $20\text{--}60 \text{ }\mu\text{m}$, and the length varies from $800\text{--}1200 \text{ }\mu\text{m}$. Therefore the devices are multimode laterally. The experiments reported here are performed on $60 \text{ }\mu\text{m}$ wide and 1.2 mm long devices. Interband lasing occurs from the ground state in the dot ($\lambda = 1.07 \text{ }\mu\text{m}$) with a threshold density of 380 A/cm^2 . The measured light (power)-current characteristics are shown in Fig. 17(a). The threshold in the MIR output occurs at 1.6 times the interband laser threshold. The additional carriers injected after the interband laser reaches threshold recombine to provide the high coherent photon density required for intersubband gain.²¹ The intersubband threshold current density is 1.1 kA/cm^2 . In essence, the device converts the more readily available near-IR photons to the more difficult to obtain mid-IR photons. While device heating prevents measurements at higher injection currents, these devices seem to demonstrate intersubband gain and dominant stimulated emission with a distinct threshold.

In an ideal spherical quantum dot, one would not expect any polarization dependence due to the symmetry of the dot shape. However since self-organized dots are very asymmetric, with the base almost three times larger than the height, a polarization dependence of the output is expected. The polarization dependence of the MIR emission is measured using a mid-infrared polarizer. The intersubband emission is found to be strongly TE polarized, as shown in Fig. 17(b). In TE polarization, the electric field vector lies in the plane of the quantum dots, whereas

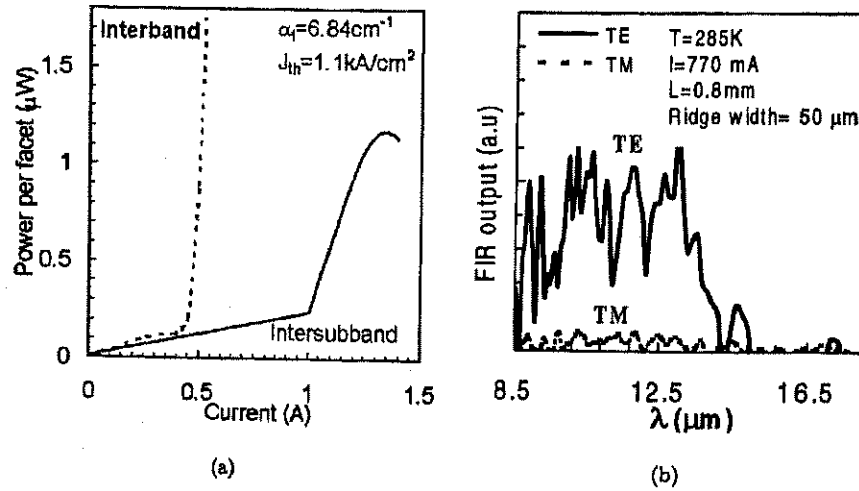


Fig. 17. (a) Light-current characteristics of the device showing a distinct threshold in the MIR emission. The interband emission is also shown for reference; and (b) the MIR output reveals a dominant TE polarization mode, which is consistent with the predictions of the eight-band $\mathbf{k} \cdot \mathbf{p}$ model.

in TM polarization, the electric field lies along the growth direction. The TE polarization of the emission is in agreement with the polarization dependence obtained using the eight-band $k \cdot p$ model.⁶⁵

Although very fine and narrow features can be resolved in the emission spectrum beyond threshold, the general shape of the spectrum still remains broad. This could be due to several reasons. The emission has always been observed to be very broad in a Fabry-Perot cavity, even in quantum cascade lasers. Design of a distributed feedback cavity could enhance the spectral purity of the output. Moreover since the ridge is very broad (60 μm), the emission is highly multimode in nature. The output power is low, and this can be enhanced with improved device design and appropriate coatings of the laser facets. Also multiple periods of QD layers could be incorporated in the active region to enhance the gain and confinement factor. The area fill factor of self-organized quantum dots is 0.25–0.3, and this low value contributes to the low confinement factor. With changes in growth techniques, the dot density can be increased by an order of magnitude.

7. Future Prospects

Phillips has made a recent comparison of the performance characteristics of MCT detectors, QWIPs, and QDIPs.⁷⁶ It is apparent from this analysis that QDIPs have the potential to outperform MCT devices. The reduction of the dark current in the vertical QDIPs, as described earlier, is very promising, but with the present heterostructure design, the photocurrent and responsivity are also reduced. In fact, increasing the responsivity of the devices is the biggest challenge. To achieve this, it is necessary to grow many more dot layers (≈ 50) without generating dislocations. Another option is to consider resonant cavity devices. Nonetheless, the demonstration of D^* approaching $10^{10} \text{ cm}^2/\text{V}$ at $T = 100 \text{ K}$ for a bias voltage of 0.2 V is very encouraging. The lateral QDIPs appear promising, as well, and further work is needed to exploit their full potential. As outlined in this chapter, QDIP focal plane arrays are yet to be realized. Single-pixel imaging is demonstrated, and this can be followed by the characterization of linear arrays. The device properties, and in particular, the responsivity, must improve before QDIPs can be incorporated in large focal plane arrays. Another important consideration for array applications is the spatial dot uniformity. The self-organization process by which the dots are formed inherently introduces a size nonuniformity, and it is yet to be seen how this affects array performance.

While great strides have been made with interband quantum dot lasers in terms of threshold current, temperature dependence, tunability of output wavelength, output power, and modulation bandwidth, the development of intersubband devices, as described in this article, is still in a nascent stage. The intersubband quantum dot light emitter described here is a bipolar device that converts interband photons to intersubband photons with a weak efficiency. Nonetheless, stimulated emission is observed, which indicates that with proper heterostructure and device

design, a significant amount of coherent light can be obtained at IR frequencies. Ultimately, a unipolar device, like the quantum cascade laser,³⁷ is desirable. However, the design of multiple periods with strained quantum dots is going to be a challenge. Nonetheless, the hurdles are not insurmountable.

Acknowledgments

This work is being supported by the Army Research Office under Grants DAAD19-01-1-0462 and DAAD19-00-1-0394 (DARPA program), as well as the National Science Foundation under Grant ECS 9820129.

References

1. K. W. Berryman, S. A. Lyon, and M. Segev, "Mid-infrared photoconductivity in InAs quantum dots", *Appl. Phys. Lett.* **70** (1997) 1861.
2. J. Phillips, K. Kamath, and P. Bhattacharya, "Far-infrared photoconductivity in self-organized InAs quantum dots", *Appl. Phys. Lett.* **72** (1998) 2020.
3. S. Kim, H. Mohseni, M. Erdtmann, E. Michel, C. Jelen, and M. Razeghi, "Growth and characterization of InGaAs/InGaP quantum dots for mid-infrared photoconductive detector", *Appl. Phys. Lett.* **73** (1998) 963.
4. S. Maimon, E. Finkman, and G. Bahir, "Intersublevel transitions in InAs/GaAs quantum dots infrared photodetectors", *Appl. Phys. Lett.* **73** (1998) 2003.
5. D. Pan, E. Towe, and S. Kennerly, "Normal-incidence intersubband (In, Ga)As/GaAs quantum dot infrared photodetectors", *Appl. Phys. Lett.* **73** (1998) 1937.
6. S. Sauvage, P. Boucaud, J. M. Gérard, and V. Thierry-Mieg, "In-plane polarized intraband absorption in InAs/GaAs self-assembled quantum dots", *Phys. Rev. B* **58** (1998) 10562.
7. S. J. Xu, S. J. Chua, T. Mei, X. C. Wang, X. H. Zhang, G. Karunasiri, W. J. Fan, C. H. Wang, J. Jiang, S. Wang, and X. G. Xie, "Characteristics of InGaAs quantum dot infrared photodetectors", *Appl. Phys. Lett.* **73** (1998) 3153.
8. Q. D. Zhuang, J. M. Li, H. X. Li, Y. P. Zeng, L. Pan, Y. H. Chen, M. Y. Kong, and L. Y. Lin, "Intraband absorption in the 8–12 μm band from Si-doped vertically aligned InGaAs/GaAs quantum-dot superlattice", *Appl. Phys. Lett.* **73** (1998) 3706.
9. A. Weber, O. Gauthier-Lafaye, F. H. Julien, J. Brault, M. Gendry, Y. Désières, and T. Benyattou, "Strong normal-incidence infrared absorption in self-organized InAs/InAlAs quantum dots grown on InP(001)", *Appl. Phys. Lett.* **74** (1999) 413.
10. N. Horiguchi, T. Futatsugi, Y. Nakata, N. Yokoyama, T. Mankad, and P. M. Petroff, "Quantum dot infrared photodetector using modulation doped InAs self-assembled quantum dots", *Jpn. J. Appl. Phys.* **38** (1999) 2559.
11. J. Phillips, P. Bhattacharya, S. W. Kennerly, D. W. Beekman, and M. Dutta, "Self-assembled InAs-GaAs quantum-dot intersubband detectors", *IEEE J. Quantum Electron.* **35** (1999) 936.
12. S. W. Lee, K. Hirakawa, and Y. Shimada, "Bound-to-continuum intersubband photoconductivity of self-assembled InAs quantum dots in modulation-doped heterostructures", *Appl. Phys. Lett.* **75** (1999) 1428.
13. L. Chu, A. Zrenner, G. Böhm, and G. Abstreiter, "Normal-incident intersubband photocurrent spectroscopy on InAs/GaAs quantum dots", *Appl. Phys. Lett.* **75** (1999) 3599.
14. D. Pan, E. Towe, and S. Kennerly, "Photovoltaic quantum-dot infrared detectors", *Appl. Phys. Lett.* **76** (2000) 3301.

15. H. C. Liu, M. Gao, J. McCafferey, Z. R. Wasilewski, and S. Fafard, "Quantum dot infrared photodetectors", *Appl. Phys. Lett.* **78** (2001) 79.
16. S. Y. Wang, S. D. Lin, H. W. Wu, and C. P. Lee, "Low dark current quantum-dot infrared photodetectors with an AlGaAs current blocking layer", *Appl. Phys. Lett.* **78** (2001) 1023.
17. A. D. Stiff, S. Krishna, P. Bhattacharya, and S. Kennerly, "High-detectivity, normal-incidence, mid-infrared ($\lambda \approx 4 \mu\text{m}$) InAs/GaAs quantum-dot detector operating at 150 K", *Appl. Phys. Lett.* **79** (2001) 421.
18. A. D. Stiff, S. Krishna, P. Bhattacharya, and S. Kennerly, "Normal-incidence, high-temperature, mid-infrared InAs-GaAs vertical quantum-dot infrared photodetector", *IEEE J. Quantum Electron.* **37** (2001) 1412.
19. L. E. Vorobev, D. A. Firsov, V. A. Shalygin, V. N. Tulupenko, Yu. M. Shernyakov, N. N. Ledentsov, V. M. Ustinov, and Zh. I. Alferov, "Spontaneous far-IR emission accompanying transitions of charge carriers between levels of quantum dots", *J. Experimental and Theor. Phys. Lett.* **67** (1998) 275.
20. S. Krishna, O. Qasalmeh, P. Bhattacharya, P. J. McCann, and K. Namjou, "Room-temperature far infrared emission from self-organized InGaAs/GaAs quantum dot laser", *Appl. Phys. Lett.* **76** (2000) 3355.
21. S. Krishna, P. Bhattacharya, P. J. McCann, and K. Namjou, "Room-temperature long-wavelength ($\lambda = 13.3 \mu\text{m}$) unipolar quantum dot intersubband laser", *Electron. Lett.* **36** (2000) 1550.
22. S. Krishna, P. Bhattacharya, J. Singh, T. Norris, J. Urayama, P. J. McCann, and K. Namjou, "Intersubband gain and stimulated emission in long wavelength ($\lambda = 13 \mu\text{m}$) intersubband quantum dot emitters", *IEEE J. Quantum Electron.* **37** (2001) 1066.
23. M. Grundmann, A. Weber, K. Goede, V. M. Ustinov, A. E. Zhukov, N. N. Ledentsov, P. S. Kop'ev, and Zh. I. Alferov, "Mid-infrared emission from near-infrared quantum dot lasers", *Appl. Phys. Lett.* **77** (2000) 4.
24. D. Klotzkin, K. Kamath, and P. Bhattacharya, "Quantum capture times at room temperature in high-speed $\text{In}_{0.4}\text{Ga}_{0.6}\text{As}$ -GaAs self-organized quantum-dot lasers", *IEEE Photonics Technol. Lett.* **9** (1997) 1301.
25. V. Ryzhii, "The theory of quantum-dot infrared phototransistors", *Semiconductor Sci. Technol.* **11** (1996) 759.
26. J. Caniou, *Passive Infrared Detection: Theory and Applications*, Kluwer Academic Publishers, Boston, 1999.
27. A. Rogalski, "Assessment of HgCdTe photodiodes and quantum well infrared photodetectors for long wavelength focal plane arrays", *Infrared Phys. Technol.* **40** (1999) 279.
28. A. Rogalski, *Infrared Detectors*, Gordon and Breach Science Publishers, Australia, 2000, pp. 155-650.
29. J. Piotrowski and W. Gawron, "Ultimate performance of infrared photodetectors and figure of merit of detector material", *Infrared Phys. Technol.* **38** (1997) 63.
30. B. F. Levine, "Quantum-well infrared photodetectors", *J. Appl. Phys.* **74** (1993) R1.
31. S. D. Gunapala and K. M. S. V. Bandara, *Heterojunction and Quantum-Well Infrared Detectors*, eds. M. H. Francombe and J. L. Vossen, Academic Press, San Diego, 1995, pp. 113-237.
32. J. L. Pan and C. G. Fonstad, Jr., "Theory, fabrication, and characterization of quantum well infrared photodetectors", *Mater. Sci. Eng. R, Reports: review j.* **28** (2000) 65.
33. M. Z. Tidrow, "Device physics and state-of-the-art of quantum well infrared photodetectors and arrays", *Mater. Sci. Eng. B* **74** (2000) 45.

34. M. Helm, P. England, E. Colas, F. DeRosa, and S. J. Allen, Jr., "Intersubband emission from semiconductor superlattices excited by sequential resonant tunneling", *Phys. Rev. Lett.* **63** (1989) 74.
35. S. Sauvage, Z. Moussa, P. Boucaud, and F. H. Julien, "Room temperature infrared intersubband photoluminescence in GaAs quantum wells", *Appl. Phys. Lett.* **70** (1997) 1345.
36. C. Sirtori, F. Capasso, J. Faist, D. L. Sivco, A. L. Hutchinson, and A. Y. Cho, "Quantum cascade unipolar intersubband light emitting diodes in the 8–13 μm wavelength region", *Appl. Phys. Lett.* **66** (1995) 4.
37. J. Faist, F. Capasso, D. Sivco, C. Sirtori, A. L. Hutchinson, and A. Y. Cho, "Quantum cascade laser", *Science* **264** (1994) 553.
38. J. Faist, F. Capasso, D. L. Sivco, A. L. Hutchinson, C. Sirtori, and A. Y. Cho, "Quantum cascade laser: A new optical source in the mid-infrared", *Infrared Phys. Technol.* **36** (1995) 99.
39. J. Faist, F. Capasso, C. Sirtori, D. Sivco, A. L. Hutchinson, S.-N. G. Chu, and A. Y. Cho, "Mid-infrared field-tunable intersubband electroluminescence at room temperature by photon-assisted tunneling in coupled-quantum wells", *Appl. Phys. Lett.* **64** (1994) 1144.
40. M. Grayson, D. C. Tsui, M. Shayegan, K. Hirakawa, R. A. Ghanbari, and H. I. Smith, "Far-infrared emission from hot quasi-one-dimensional quantum wires in GaAs", *Appl. Phys. Lett.* **67** (1995) 1564.
41. O. Gauthier-Lafaye, P. Boucaud, F. H. Julien, S. Sauvage, S. Cabaret, and J. M. Lourtioz, "Long-wavelength ($\sim 15.5 \mu\text{m}$) unipolar semiconductor laser in GaAs quantum wells", *Appl. Phys. Lett.* **71** (1997) 3619.
42. P. J. McCann, K. Namjou, and X. M. Fang, "Above-room-temperature continuous-wave mid-infrared photoluminescence from PbSe/PbSrSe quantum wells", *Appl. Phys. Lett.* **75** (1999) 3608.
43. H. Benisty, C. M. Sotomayor-Torres, and C. Weisbuch, "Intrinsic mechanism for the poor luminescence properties of quantum-box systems", *Phys. Rev. B* **44** (1991) 10945.
44. L. Goldstein, F. Glas, J. Y. Marzin, M. N. Charasse, and G. Leroux, "Growth by molecular beam epitaxy and characterization of InAs/GaAs strained-layer superlattices", *Appl. Phys. Lett.* **47** (1985) 1099.
45. D. Leonard, M. Krishnamurthy, C. M. Reaves, S. P. Denbaars, and P. M. Petroff, "Direct formation of quantum-sized dots from uniform coherent islands of InGaAs on GaAs surfaces", *Appl. Phys. Lett.* **63** (1993) 3202.
46. J. Pamulapati, P. K. Bhattacharya, J. Singh, P. R. Berger, C. W. Snyder, B. G. Orr, and R. L. Tober, "Realization of *in-situ* sub two-dimensional quantum structures by strained layer growth phenomena in the $\text{In}_x\text{Ga}_{1-x}\text{As}/\text{GaAs}$ system", *J. Electron. Mater.* **25** (1996) 479.
47. S. Guha, A. Madhukar, and K. C. Rajkumar, "Onset of incoherency and defect introduction in the initial stages of molecular beam epitaxy growth of highly strained $\text{In}_x\text{Ga}_{1-x}\text{As}$ on GaAs (100)", *Appl. Phys. Lett.* **57** (1990) 2110.
48. J. M. Moison, L. Leprince, F. Barthe, F. Houzay, N. Lebouche, J. M. Gerard, and J. Y. Marzin, "Self-organized growth of InAs/GaAs quantum boxes", *Appl. Surface Sci.* **92** (1996) 526.
49. N. P. Kobayashi, T. R. Ramachandran, P. Chen, and A. Madhukar, "*In-situ*, atomic force microscope studies of the evolution of InAs three-dimensional islands on GaAs (001)", *Appl. Phys. Lett.* **68** (1996) 3299.

50. Q. Xie, P. Chen, A. Kalburge, T. R. Ramachandran, A. Nayfonov, A. Konkar, and A. Madhukar, "Realization of optically active strained InAs island quantum boxes on GaAs (100) via molecular beam epitaxy and the role of island induced strain fields", *J. Crystal Growth* **150** (1995) 357.
51. J. Y. Marzin, J. M. Gerard, A. Izrael, and D. Barrier, "Photoluminescence of single InAs quantum dots obtained by self-organized growth on GaAs", *Phys. Rev. Lett.* **73** (1994) 716.
52. S. Fafard, D. Leonard, J. L. Merz, and P. M. Petroff, "Selective excitation of photoluminescence and the energy levels of ultrasmall InGaAs/GaAs quantum dots", *Appl. Phys. Lett.* **65** (1994) 1388.
53. G. Wang, S. Fafard, D. Leonard, J. L. Merz, and P. M. Petroff, "Time-resolved optical characterization of InGaAs/GaAs quantum dots", *Appl. Phys. Lett.* **64** (1994) 2815.
54. M. Grundmann, "InAs/GaAs quantum dots radiative recombination from zero-dimensional states", *Phys. Status Solidi* **188** (1995) 249.
55. D. I. Lubyshv, P. P. Gonzales-Borrero, E. Marega, E. Petitprez, N. Lascala, and P. Basmaji, "Exciton localization and temperature stability in self-organized InAs quantum dots", *Appl. Phys. Lett.* **68** (1996) 205.
56. R. Heitz, M. Grundmann, N. N. Ledentsov, L. Eeckey, M. Veit, D. Bimberg, V. M. Ustinov, A. Egorov, A. E. Zhukov, P. S. Kop'ev, and Z. I. Alferov, "Multiphonon relaxation processes in self-organized InAs/GaAs quantum dots", *Appl. Phys. Lett.* **68** (1996) 361.
57. M. Grundmann, N. N. Ledentsov, O. Stier, D. Bimberg, V. M. Ustinov, P. S. Kop'ev, and Z. I. Alferov, "Excited states in self-organized InAs/GaAs quantum dots: Theory and experiment", *Appl. Phys. Lett.* **68** (1996) 979.
58. K. Kamath, P. Bhattacharya, and J. Phillips, "Room temperature luminescence from self-organized $\text{In}_x\text{Ga}_{1-x}\text{As}/\text{GaAs}$ ($0.35 < x < 0.45$) quantum dots with high size uniformity", *J. Crystal Growth* **175-176** (1997) 720.
59. K. Kamath, N. Chervela, K. K. Linder, T. Sosnowski, H. T. Jiang, T. Norris, J. Singh, and P. Bhattacharya, "Photoluminescence and time-resolved photoluminescence characteristics of $\text{In}_x\text{Ga}_{1-x}\text{As}/\text{GaAs}$ self-organized single- and multiple-layer quantum dot laser structures", *Appl. Phys. Lett.* **71** (1997) 927.
60. I. N. Stranski and L. V. Krastanov, *Akad. Wiss. Lett. Mainz Math. Natur.* **146** (1939) 797.
61. P. R. Berger, K. Chang, P. Bhattacharya, J. Singh, and K. K. Bajaj, "Role of strain and growth conditions on the growth front profile of $\text{In}_x\text{Ga}_{1-x}\text{As}$ on GaAs during the pseudomorphic growth regime", *Appl. Phys. Lett.* **53** (1988) 684.
62. V. A. Shchukin, N. N. Ledentsov, P. S. Kop'ev, and D. Bimberg, "Spontaneous ordering of arrays of coherent strained islands", *Phys. Rev. Lett.* **75** (1995) 2968.
63. Q. Xie, A. Madhukar, P. Chen, and N. P. Kobayashi, "Vertically self-organized InAs quantum box islands on GaAs (100)", *Phys. Rev. Lett.* **75** (1995) 2542.
64. G. S. Solomon, J. A. Trezza, A. F. Marshall, and J. S. Harris, Jr., "Vertically aligned and electronically coupled growth induced InAs islands in GaAs", *Phys. Rev. Lett.* **76** (1996) 952.
65. H. Jiang and J. Singh, "Strain distribution and electronic spectra of InAs/GaAs self-assembled dots: An eight-band study", *Phys. Rev. B* **56** (1996) 4696.
66. T. Sosnowski, T. Norris, H. Jiang, J. Singh, K. Kamath, and P. Bhattacharya, "Rapid carrier relaxation in $\text{In}_{0.4}\text{Ga}_{0.6}\text{As}/\text{GaAs}$ quantum dots characterized by differential transmission spectroscopy", *Phys. Rev. B* **57** (1998) R9423.

67. J. Urayama, T. B. Norris, J. Singh, and P. Bhattacharya, "Observation of phonon bottleneck in quantum dot electronic relaxation", *Phys. Rev. Lett.* **86** (2001) 4930.
68. H. C. Liu, "Noise gain and operating temperature of quantum well infrared photo-detectors", *Appl. Phys. Lett.* **61** (1992) 2703.
69. W. A. Beck, "Photoconductive gain and generation-recombination noise in multiple-quantum-well-infrared detectors", *Appl. Phys. Lett.* **63** (1993) 3589.
70. J. Singh, "Possibility of room temperature intra-band lasing in quantum dot structures placed in high-photon density cavities", *IEEE Photonics Technol. Lett.* **8** (1996) 488.
71. A. Kastalsky, L. E. Vorobjev, D. A. Firsov, V. L. Zerova, and E. Towe, "A dual-color injection laser based on intra- and inter-band carrier transitions in semiconductor quantum wells or quantum dots", *IEEE J. Quantum Electron.* **37** (2001) 1356.
72. H. T. Jiang and J. Singh, "Conduction band spectra in self-assembled InAs/GaAs dots: Comparison of effective mass and an eight-band approach", *Appl. Phys. Lett.* **71** (1997) 3239.
73. J. Singh, *Physics of Semiconductors and Their Heterostructures*, McGraw-Hill Inc., New York, 1993.
74. K. Nishi, H. Saito, S. Sugou, and J.-S. Lee, "A narrow photoluminescence linewidth of 21 meV at 1.35 μm from strain-reduced InAs quantum dots covered by $\text{In}_{0.2}\text{Ga}_{0.8}\text{As}$ grown on GaAs substrate", *Appl. Phys. Lett.* **74** (1999) 1111.
75. G. Abstreiter, "Micro-Raman spectroscopy for characterization of semiconductor devices", *Appl. Surface Sci.* **50** (1991) 73.
76. J. Phillips, "Evaluation of the fundamental properties of quantum dot infrared detectors", to be published in *J. Appl. Phys.* **91** (2002).